Food Chemistry: X 22 (2024) 101471

Contents lists available at ScienceDirect

Food Chemistry: X

journal homepage: www.sciencedirect.com/journal/food-chemistry-x

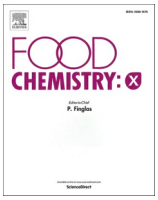

Poly (ionic liquid) cross-linked hydrogel encapsulated with AuPt nanozymes for the smartphone-based colorimetric detection of zearalenone

Qianwen Liu, Lingling Zhou, Siyu Xin, Qingli Yang, Wei Wu, Xiudan Hou *

College of Food Science and Engineering, Qingdao Agricultural University, Qingdao 266109, China

ARTICLE INFO

Keywords:
Ionic liquid
Hydrogel
Colorimetric biosensor
AuPt
Smartphone

ABSTRACT

A poly (ionic liquid) enhanced poly(acrylamide-acrylic acid) (PIL-PAM/AA) hydrogel-based colorimetric sensor was designed to detect zearalenone (ZEN). Different Au_xPt_y nanoparticles were synthesized via the on-pot method. Through the kinetic analysis and the theoretical calculation, $Au_{0.4}Pt_{0.6}$ possessed the relatively low energy barriers to adsorb and decompose H_2O_2 so that it exhibited relatively better catalytic activity ($K_m = 2.02 \times 10^{-3}$, $V_{max} = 6.14 \times 10^{-7}$). AuPt nanoparticles were encapsulated into PIL-PAM/AA hydrogel via the interaction between aptamer and cDNA. In the presence of ZEN, the embedded AuPt nanoparticles were released to complete the catalytic reaction. Coupled with the smartphone application, the established method provided the linear range of 1–250 ng mL^{-1}, with a detection limit of 0.6979 ng mL^{-1} for ZEN. Meanwhile, it also possessed excellent selectivity and good anti-interference performance. In wheat and corn samples, spiked recoveries were ranging from 75% to 113.30%.

1. Introduction

Zearalenone (ZEN), also known as F-2 toxin, is a secondary metabolite produced by Fusarium and a kind of female mycotoxin (Ma, Guo, Ye, Zhang, & Wang, 2023). It is widely distributed in moldy corn, wheat, oats and other grain (Zhang, Chen, Lu, Yu, & Zhang, 2023). ZEN and its derivatives can damage human reproductive and digestive systems, and ZEN has been classified as a Group III carcinogen, which can cause serious economic losses to the agriculture and food industry (Tan et al., 2020). At present, ZEN has been mainly detected by the traditional methods focusing on gas chromatography, high performance liquid chromatography, and gas/liquid chromatography-mass spectrometry (Li et al., 2023). They have high sensitivity and stability, but the conventional chromatography-mass spectrometry technologies have disadvantages of high cost, long detection time, expensive equipment, large solvent consumption, especially being unable to conduct on-site detection (Yang et al., 2022). Therefore, there are many inconveniences for the supervision of agricultural and sideline products.

Hydrogel is a hydrophilic three-dimensional network gel composed of single or mixed hydrated polymers, which includes natural polymer hydrogels (i.e., cellulose, chitosan, etc.), synthetic polymer hydrogels (i.e., polyacrylamide, polyethylene glycol, etc.), and hybrid polymer hydrogels (Wang et al., 2024). Hydrogels possesses good flexibility, water retention, chemical stability and biocompatibility (Zhou, Fei, Tian, Xu, & Li, 2022). The porous network structure of hydrogels is naturally conducive to carry drugs and realize the release of targets through the change of pressure, temperature, pH, light and electrical stimulation (Qu et al., 2023), so hydrogels have been widely used in tumor therapy, wound dressing and bioelectronics (Fang et al., 2019). In recent years, hydrogels have been used as support materials for nanozymes due to their elastic and soft natural properties (Lv, Liu, Shao, Song, & Sun, 2020). Moreover, hydrogels with porous network structure were beneficial for the in-situ synthesis and encapsulation of other nanoparticles (Wang et al., 2023). However, due to the weak interaction and incompatibility, it would lead to insufficient monomers polymerization and poor loading capacity. Ionic liquids (ILs) with various asymmetric ions, possess remarkable properties of non-volatile, antibacterial, thermal stability, etc. (Lu et al., 2022). The structure of ILs can be adjusted by the design of cation and anion to regulate the related properties including stability, hydrophilicity/hydrophobicity, viscosity, density, and solubility (Lv et al., 2021). ILs, as microextraction solvents, can also be modified and functionalized to enhance specific interactions with analytes and improve extraction efficiency. Due to its non-volatility, it is not suitable for equipment such as chromatographs and atomic absorption (Ahmadi, Azooz, Yamini, & Ramezani, 2023; Semysim, Ridha, Azooz, & Snigur, 2024). It is thus clear that the high

* Corresponding author.
E-mail address: qdxdhou@qau.edu.cn (X. Hou).

https://doi.org/10.1016/j.fochx.2024.101471
Received 8 April 2024; Received in revised form 7 May 2024; Accepted 13 May 2024
Available online 16 May 2024

selectivity of polymer fragments and high designability of ILs would enlarge the applications. The introduction of ILs into the hydrogel could endow them with higher solubility and excellent mechanical properties (Qu et al., 2023). Besides, due to the electrostatic and π-π interaction, the encapsulated capacity of ILs cross-linked hydrogels towards other nanoparticles would be also improved (Karimi-Maleh et al., 2021). Lv et al. successfully synthesized polyacrylamide/dimethylaminoethyl methacrylate bromododecane hydrogel with poly(ionic liquids) microspheres, which was acted as a template for loading Pd nanoparticles without the addition of crosslinking agents and other additives (Lv, Lv, Tian, Xie, & Sun, 2023). The meal-laden hydrogel exhibited excellent catalytic efficiency for the reduction of 4-nitrophenol. Ji et al. prepared hydrogel particles with different shapes as coding elements, which was used to detect mycotoxin on the basis of the stop-flow lithography technology. The image recognition programs installed on smart phones to analyze images for OTA/AFB1 detection (Ji et al., 2019).

In recent years, nanozymes with natural enzyme properties have been developed in many fields ranging from biosensing to imaging, therapy. The studied nanozymes mainly included oxidase, peroxidase, catalase, superoxide dismutase, phosphatase mimics (Bian et al., 2023). On the basis of the inherent property, nanozymes can also be used as recognition receptors and signal probes (Gai, Pu, Wang, Zhu, & Li, 2023). Noble metal-based peroxidase mimics are favored since they can accept and donate electrons in redox catalytic reactions (Amor et al., 2023). Generally, bimetallic nanoparticles were significantly superior to monometallic nanoparticles in view of catalytic activity and stability (Shao et al., 2019). AuPt nanoparticles have excellent optical properties and catalytic activity, and are widely used in fields such as catalysis, biosensing, and therapy (Wei, Zhang, Chen, & Zeng, 2020). Qiao et al. successful synthesized Pt—Au nanoflowers with the core-shell structure, which combined with monoclonal antibodies as signal probes for the sensitive detection of ZEN (Qiao et al., 2024).

Hydrogels can incorporate various crosslinkers including deoxyribonucleic acid (DNA). Firstly, this work synthesized poly(ionic liquid) (PIL) crosslinked poly(acrylamide-acrylic acid) (PAM/AA) hydrogel via a ultrasonic-assisted radical polymerization. Different Au_xPt_y nanoparticles were also prepared via the on-pot method to optimize the peroxidase-like catalytic activity. PIL crosslinked PAM/AA hydrogels encapsulated with AuPt nanozymes were prepared as the target-response and signal-amplification materials to establish an ultrasensitive colorimetric platform for the on-site detection of ZEN coupling with smartphone-based image acquisition. The existence of ZEN would compete with aptamer and lead to the dissociation of aptamer and cDNA, thereby causing the hydrogel collapse and releasing encapsulated AuPt nanozymes to produce catalyzed reaction and visual signal.

2. Materials and methods

2.1. Materials and reagents

Hydrogen peroxide (H_2O_2), glacial acetic acid (HAc), 3,3′,5,5′-tetramethylbenzidine (TMB), chloroauric acid ($HAuCl_4$), potassium chloroplatinate (K_2PtCl_6), trisodium citrate and acrylamide (AM) were obtained from Macklin Biochemical Co., Ltd. (Shanghai, China). Dimethyl sulfoxide (DMSO) was purchased from National Pharmaceutical Co., Ltd. (Shanghai, China). ZEN was obtained from Pribon Technology Co., Ltd. (Qingdao, China). 1-Allyl-3-butyl imidazole bromide ($ABIm^+Br^-$) was obtained from Aolike New Material Technology Co., Ltd. (Qingdao, China). Ammonium Persulfate (APS, 99%), *N*, *N*′-methylene bisacrylamide (MBA, 99%), tetramethylethylenediamine (TEMED) and acrylic acid (AA, 98%) were obtained from Adamas-beta (Shanghai, China). *N*-Hydroxy succinimide (NHS), and *N*-(3-dimethylaminopropyl)-*N*-ethylcarbodiimide (EDC) were bought from Aladdin Chemical Reagent Co., Ltd. (Shanghai, China). Aptamer and complementary DNA were synthesized by Sangon Biotech Co., Ltd. (Shanghai, China), and the chain sequences were as follows:

Aptamer: GATGTCATCTATCTATGGTACATTACTATCTGTAATGTGATATGCCTA
cDNA1: 5 '-COOH-TTTTTTTAGGCATATCAC-3'
cDNA2: 5 '-COOH-TTTTTTATAGATGACATC-3'

2.2. Equipment

The morphology and structure of hydrogels were observed by scanning electron microscope (SEM, JSM-6701S, Hitachi, Japan). Functional groups of different hydrogels were compared by Fourier infrared spectrum (FTIR, Nicolet 10, Thermo, USA), FTIR measurements were conducted in absorbance mode within the range of 400–4000 cm^{-1}, with a resolution of 0.09 cm^{-1}. The hydrophobic angle of hydrogels was measured by Contact angle measurement instrument (OCA, DSA100S, KRÜSS, Germany). The mechanical properties of hydrogels were observed by electronic universal testing machine (UTM, CTM2500, Xieqiang, China). The structure of AuPt nanoparticles were characterized by transmission electron microscopy (TEM, Hitachi, Japan), atomic force microscope (AFM, SPM-9700 HT, Shimadzu, Japan), X-ray photoelectron spectroscopy (XPS, EScalab 250xi, Thermo, USA). Besides, the catalytic capacity of nanozyme was detected and recorded by ultraviolet-visible spectrophotometer (UV–Vis, Evolution 201, Thermo Scientific Instruments, Inc., USA) and a microplate reader (Multiskan FC, Thermo, USA).

2.3. Preparation of PIL crosslinked hydrogels

Firstly, a certain amount of $ABIm^+Br^-$ was added into 1.2 mL ultrapure water for ultrasonically dispersing into a homogeneous solution. Then, 0.8 mL of AA, 0.4 g AM, 0.01 g MBA, 0.02 g APS and 10 μL of TMEDA were added to the above solution. The homogeneous mixture was reacted at 65 °C under ultrasound and continuously heat for 30 min to complete the polymerization. After that, hydrogels were soaked in ultrapure water at 50 °C for 12 h, which were repeated 3 times to remove the residual, and then stored in ultrapure water or humid environment. The content of $ABIm^+Br^-$ added in the hydrogel were 6%, 8%, 10%, 12%, 14%.

2.4. Preparation of AuPt nanoparticles

AuPt nanoparticles were synthesized according to the literature (Song, Li, Bai, Gai, & Li, 2022). 5 Milliliters of $HAuCl_4$ solution (4 mM) and 5 mL of K_2PtCl_6 solution (6 mM) were placed into a beaker, stirring for 5 min to obtain the homogeneous mixture. After heating to boil (100 °C), 5 mL of trisodium citrate (20 mg mL^{-1}) was added and continuously heated for 10 min to obtain AuPt nanoparticles.

2.5. Encapsulation of AuPt nanoparticles in DNA hydrogel

Firstly, 2 μL of EDC (2 mM) and 2 μL of NHS (5 mM) were mixed to stand for 1 h at 4 °C to activate carboxyl groups. Then, the hydrogel with the cube length of 3 mm was placed into the above mixed solution to immobilize DNA through the amide reaction. After 30 min at 65 °C, 10 μL of aptamer (10 μM), 10 μL of COOH-cDNA1 (10 μM), 10 μL of COOH-cDNA2 (10 μM) and 200 μL of AuPt nanoparticles suspension were added to encapsulate AuPt nanoparticles inside hydrogel (Bian et al., 2023).

2.6. Evaluation of peroxidase-like activity

The enzymatic kinetic activity of different AuPt nanoparticles was studied with different concentrations of TMB and H_2O_2. When TMB (10 mM) was used as the substrate, a certain amount of AuPt nanoparticles was incubated with 160 μL of HAc-NaAc buffer (pH = 4.5) and 80 μL of H_2O_2 (100 mM) for 3 min, and the colorless TMB would change to blue oxTMB. The absorbance values at 652 nm were recorded by UV–Vis

spectroscopy. Finally, the Michaelis-Menten equation was used to plot the relationship of absorbance and concentration. The related kinetic parameters were also calculated according to the equation: $1/V = (K_m/V_{max})\ (1/[S]) + 1/V_{max}$, where V is the initial reaction rate, V_{max} is the maximum reaction rate, $[S]$ is the substrate concentration, and K_m is the Michaelis-Menten constant.

2.7. Evaluation of swelling and water loss rate

In order to evaluate the water absorption and retention of hydrogels, the swelling and water loss rate were evaluated (Gao et al., 2023; Gilarska, Lewandowska-Łańcucka, Horak, & Nowakowska, 2018). The hydrogel sample was placed into a vacuum oven at 37 °C to dry until the constant weight. Then it was put into deionized water to absorb water for swelling until the equilibrium. The hydrogel was taken out at intervals to wipe water on the surface and record weight (W_e, e = 0, 5, 10, 20, 40, 60, 100 min). The swelling ratio (Q) was defined as: $Q = (W_e\text{-}W_0)/W_0 \times 100\%$, where W_e and W_0 are the weight of hydrogels before and after water uptake, respectively. The weight of the hydrogel at swelling balance was recorded as W_c. It was dried at a vacuum oven and the weight in different intervals (W_t, t = 0.5, 1, 1.5, 2, 3, 4, 6, 8, 10, 12, 22, 24 h) was recorded. The water loss rate (M) was calculated as: $M = (W_c\text{-}W_t)/W_c \times 100\%$.

2.8. Density functional theory calculation

All the calculations were carried out by means of spin-polarized density functional theory (DFT) method using Vienna Ab-initio Simulation Package. The exchange and correlation energies were described by the generalized gradient approximation with the Perdew-Burke-Ernzerhof functional. The projector augmented-wave method was used to describe the electron-ion interactions. The detailed information was described in Supplementary Material.

2.9. Sample pretreatment

Wheat and corn were purchased from the local supermarket (Qingdao, China). The samples were crushed into powder using a grinder, and 1 g of the crushed sample was added in a mixed solution of acetonitrile and water (10 mL, 8:2), which was extracted and sonicated for 1 h. The supernatant was taken and dried under the N_2 atmosphere, and resolved in 10 mL of ultrapure water. It was filtered by 0.45 μM, 0.22 μM membrane to be detected.

3. Results and discussion

3.1. The detection mechanism of colorimetric sensors

The encapsulated AuPt nanozymes hydrogel was prepared as a signal response element to establish ultrasensitive colorimetric platform for the on-site detection of ZEN. When ZEN was added, it would preferentially combine with the aptamer to compete with the cDNA, which resulted in the loose internal structure of the hydrogel and the release of AuPt nanozymes. The released AuPt nanozymes would catalyze the decomposition of H_2O_2 to oxidize the colorless TMB to blue oxTMB, thereby achieving qualitative and quantitative detection of ZEN (Scheme 1).

3.2. Characterization of the hydrogel and AuPt nanoparticles

The morphology of freeze-dried PIL-AM/AA hydrogel was characterized by SEM. Fig. 1 (A, B) exhibited that the hydrogel possessed a typical porous three-dimensional network structure, and the pore size was approximately 0.1–1.4 μm, which was conducive to the loading of AuPt nanozymes. The functional groups of PIL-AM/AA hydrogel were characterized by FT-IR. As shown in Fig. 1D, there were adsorption peaks of N—H stretching vibration at 3350 cm^{-1}, saturated C—H at 2950 cm^{-1}, C═C at 1710 cm^{-1} and C═O 1640 cm^{-1} (Fang et al., 2019; Karimi-Maleh et al., 2021; Ramezani et al., 2024). Compared with PAM/AA hydrogel, PIL-AM/AA hydrogel appeared the corresponding peaks of

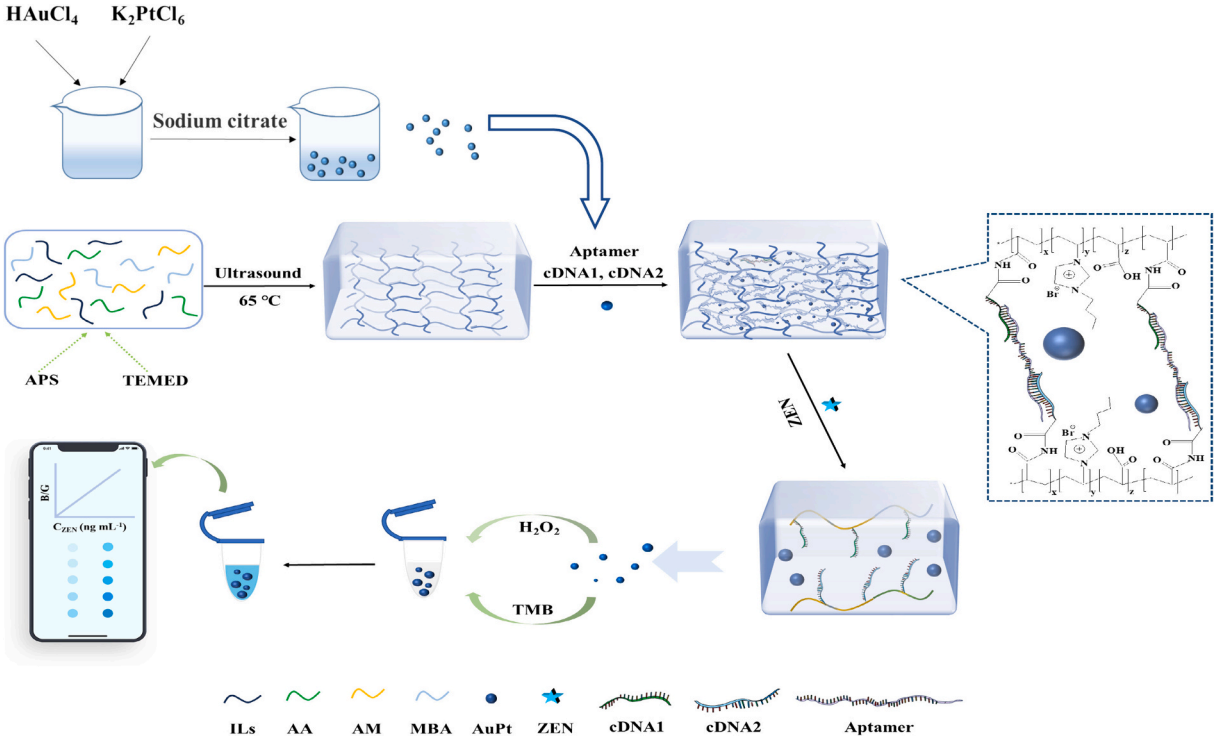

Scheme 1. Schematic illustration of poly(ionic liquid) cross-linked hydrogel encapsulated with AuPt nanozymes for colorimetric detection of zearalenone.

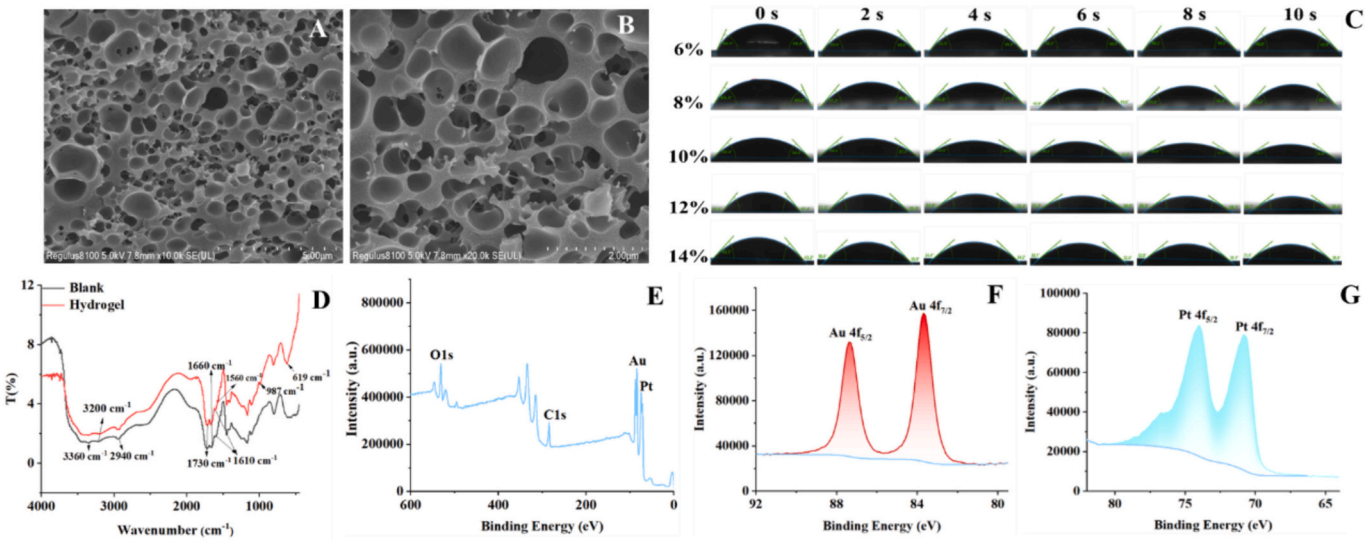

Fig. 1. (A, B) SEM images of hydrogel. (C) The contact angle measurement of hydrogel between 0 s and 10 s. (D) FTIR characterization of hydrogel. (E) XPS spectra of $Au_{0.4}Pt_{0.6}$ nanoparticles. The high resolution XPS spectra of (F) Au 4 f and (G) Pt 4 f.

PIL, which were C═N stretching vibration at 1590 cm^{-1} and the bending vibration of imidazole ring at 987 cm^{-1}. It proved the successful polymerization of ILs with AM/AA.

The morphology of AuPt nanoparticles were characterized by TEM. It was observed from Fig. 2 (C, D) that AuPt nanoparticles possessed the spraying flower-like structure. The element mapping images described the uniform distribution of Au and Pt elements on AuPt nanoparticles (Fig. 2). The AFM image also exhibited the nearly spherical structure (Fig. 2H). The size of AuPt nanoparticles was approximately 30 nm, and the distribution profile was listed in Fig. 2G. As shown in Fig. 1(E-G), the XPS spectra showed the peaks of Au 4 $f_{5/2}$ and Au 4 $f_{7/2}$ at 87.2 eV and 83.6 eV, and the peaks of Pt 4 $f_{5/2}$ and Pt 4 $f_{7/2}$ at 73.9 eV and 70.7 eV, respectively. Compared with Au 4 $f_{7/2}$ and Pt 4 $f_{7/2}$, the shift of binding energies further verified to interaction between Au and Pt (Wang, Lin, Li, Lu, & Peng, 2019).

The modification of cDNA and connection of aptamer were verified through an electrophoresis experiment. As shown in Fig. S1, Lane 4 was the combination of cDNA1, Apt, and cDNA2, and its molecular weight was larger than that of Lane 2 (cDNA1) and Lane 3 (cDNA2), indicating that aptamer was successfully connected with two complementary chains. Lane 5 was darker than Lane 4, resulted from that a part of cDNA1 + Apt+cDNA2 combined with hydrogel, resulting in a decrease of cDNA1 + Apt+cDNA2 in the supernatant.

3.3. Properties of the PIL-AM/AA hydrogel

3.3.1. Transparency and water contact angle

As shown in Fig. S2, hydrogels exhibited a switchable optical behavior with the change of IL content and temperature. With the increase of ILs, the transparency gradually became opaque. And the PIL-AM/AA hydrogel possessed higher transparency at 60 °C than that at room temperature. To explore the transparency transformation mechanism, the water contact angle of hydrogels with different concentrations was investigated and exhibited in Fig. 1C. When the IL content was 6%,

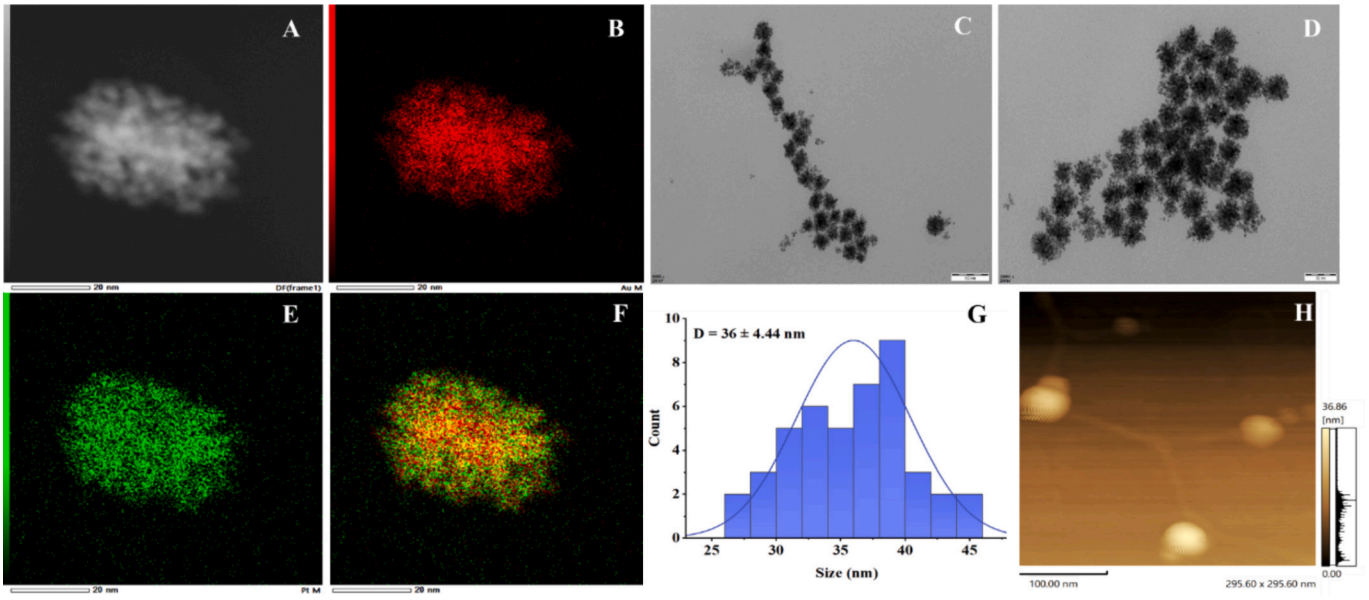

Fig. 2. (A, B, E, F) HAADF-STEM image and EDX elemental mapping of $Au_{0.4}Pt_{0.6}$ nanoparticles. (C, D) TEM images of $Au_{0.4}Pt_{0.6}$ nanoparticles. (G) Particle size distribution histogram of $Au_{0.4}Pt_{0.6}$ nanoparticles. (H) AFM image of $Au_{0.4}Pt_{0.6}$ nanoparticles.

8%, 10%, 12%, 14%, contact angles of hydrogels were 69.7°, 65.3°, 52.4°, 47.5°, and 43.3°, respectively. With the increase of ILs content, the water contact angle of hydrogels gradually decreased, indicating that the hydrophilicity increased with the addition of ILs. Within 10s, the water contact angle of hydrogels gradually decreased, which was resulted from that water would flow along the PIL-AM/AA hydrogel network and quickly entered the interior of hydrogels.

3.3.2. Water content and swelling properties

The swelling ratio is an important parameter to characterize the network structure of hydrogels (Gilarska et al., 2018). The swelling ratio depends on the degree of network crosslinking and the number of hydrogen bonds of hydrogels. Fig. S3A showed that within 20 min, the swelling ratio of the hydrogel rapidly increased and then tended to stabilization. And with the increase of ILs, the swelling ratio decreased, which was resulted from that a dense network structure was formed inside the hydrogel, and water was not easy to diffuse in the hydrogel to lead to the reduction of the swelling ratio.

Water retention (water loss rate) was also one of the key properties of hydrogels (Gao et al., 2023). It could be found that with the increase of ILs, the water loss rate of hydrogels increased and the water retention decreased (Fig. S3B). Generally, the water holding capacity of hydrogels was >65%, which proved that the prepared hydrogels had good water holding capacity.

3.3.3. Mechanical properties of hydrogels

Excessive ILs can hinder the formation of multiple network structures (Qu et al., 2023). Therefore, the optimization of ILs content was a key step to reach the desirable mechanical elasticity. The tensile properties of hydrogels with different ILs (6%, 8%, 10%, 12%, 14%) were investigated using a universal testing machine. Fig. S4 showed that as the content of ILs increased, the mechanical properties increased. The hydrogel with 6% ILs was the shortest tensile displacement, and the hydrogel with 14% ILs was the longest tensile displacement. However, the hydrogel containing 14% ILs was relatively soft, which was not suitably utilized for the detection, so 8% was selected as the optimal content of ILs.

3.3.4. Adhesion

As shown in Fig. S5, the PIL-AM/AA hydrogel exhibited excellent self-adhesive performance towards such commonly materials (wood, dovetail clip, rubber, cent coin, plastics, etc.). It could be assigned to the physical effect between hydrogels and materials. The self-adhesive property was important for recycling and long-time using. The adhesion of capture materials was important for the detection materials applied in the solid samples. Therefore, it possessed the potential in directly detection in real samples.

3.4. Kinetic analysis of AuPt nanozymes

The peroxidase-like catalytic activities of different types of Au_xPt_y nanoparticles were investigated and evaluated through the oxidation of TMB by H_2O_2 as a model reaction. As shown in Fig. 3A, it would yield a blue-colored oxTMB as the product with an adsorption wavelength of 652 nm to be conveniently recorded and quantified by a UV–Vis spectrophotometer. Fig. 3B exhibited that the peroxidase-like catalytic activity of Au_xPt_y nanoparticles was obviously higher than that of Au@Pt and Pt@Au nanoparticles. For comparison, the catalytic activity of different ratios of Au and Pt atoms (1:9, 2:8, 3:7, 4:6, 5:5, 6:4, 7:3, 8:2, 9:1) were also determined. With the increase of Au atom, the UV–Vis adsorption value firstly increased and then reduced, and $Au_{0.4}Pt_{0.6}$ presented highest catalytic activity (Fig. 3C). Peroxidase-like activities of five ratios of Au_xPt_y nanoparticles were evaluated by the steady-state kinetic assays. The initial reaction velocity against TMB concentration was plotted to obtain five typical Michaelis-Menten curves (Fig. 3D). These curves were then converted to the double-reciprocal plots, from which V_{max}, K_m and K_{cat} values were derived for the plotting curves. As shown in Fig. 3E, K_{cat} values of Au_xPt_y nanoparticles presented a volcano-shaped dependence on the increase of Au content, with the maximum point corresponding to $Au_{0.4}Pt_{0.6}$. Table 1 also listed and compared the related kinetic parameters of different Au_xPt_y nanoparticles and other reported nanozymes towards the oxidation of TMB by H_2O_2. K_m (2.02×10^{-3} M) and K_{cat} (3.06×10^6 S^{-1}) values of $Au_{0.4}Pt_{0.6}$ nanoparticles were obviously higher than those of other Au_xPt_y nanoparticles, which demonstrated that $Au_{0.4}Pt_{0.6}$ nanoparticles possessed strong affinity towards H_2O_2. Compared with other reported nanozymes, the prepared $Au_{0.4}Pt_{0.6}$ nanoparticles also exhibited an advantage in the TMB/H_2O_2 reaction.

To demonstrate the origin of the excellent peroxidase-like catalytic efficiency of AuPt nanoparticles, spin-polarized density functional

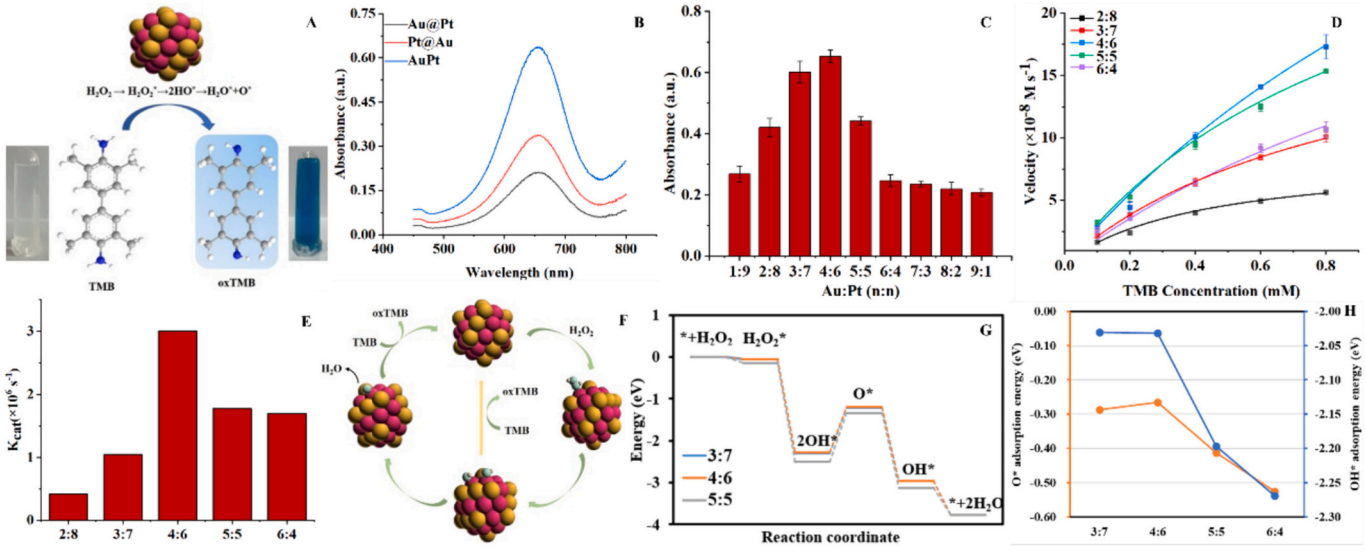

Fig. 3. (A) Schematics showing the catalytic oxidation of TMB by H_2O_2. (B) The absorbance spectrum of different materials. (C) Optimization of molar ratio of AuPt nanoparticles. (D) Plots of initial reaction velocity for different AuPt nanoparticles against TMB concentration. (E) K_{cat} of different AuPt nanoparticles. (F) Proposed H_2O_2 decomposition pathway on $Au_{0.4}Pt_{0.6}$ nanoparticles. (G) Free-energy diagrams for H_2O_2 decomposition on Au_xPt_y surfaces and optimized adsorption configurations on AuPt surface. (H) Adsorption energies for OH* and O* on the AuPt slab model surfaces.

Table 1
Comparison of kinetic parameters better different AuPt nanoparticles prepared in this work nanozymes reported in other literature.

Catalyst	Substrate	K_m (M)	V_{max} (M s^{-1})	K_{cat} (S^{-1})	Ref.
HRP	TMB	4.34×10^{-4}	1.00×10^{-7}	4.30×10^{3}	(Gao et al., 2007)
Au NPs	TMB	1.00×10^{-2}	2.82×10^{-7}	3.67×10^{2}	(Khoris et al., 2019)
Pt NPs	TMB	4.8×10^{-4}	7.90×10^{-7}	9.70×10^{5}	(Xi et al., 2021)
Au_2Pt	TMB	4.40×10^{-5}	1.94×10^{-7}	–	(Wu et al., 2023)
AuPtRh	TMB	6.63×10^{-4}	$2.0.22 \times 10^{-7}$	–	(Tan et al., 2022)
$Au_{0.2}Pt_{0.8}$	TMB	4.29×10^{-4}	8.60×10^{-8}	4.15×10^{5}	This work
$Au_{0.3}Pt_{0.7}$	TMB	9.11×10^{-4}	2.14×10^{-7}	1.04×10^{6}	This work
$Au_{0.4}Pt_{0.6}$	TMB	2.02×10^{-3}	6.14×10^{-7}	3.06×10^{6}	This work
$Au_{0.5}Pt_{0.5}$	TMB	1.00×10^{-3}	3.46×10^{-7}	1.77×10^{6}	This work
$Au_{0.6}Pt_{0.4}$	TMB	1.83×10^{-3}	3.61×10^{-7}	1.70×10^{6}	This work

Horseradish peroxidase (HRP); Nanoparticles (NPs).

theory (DFT) methods were used to calculate and analysis for H_2O_2 decomposition on different Au_xPt_y surfaces. According to the reported work, the decomposition mechanism of H_2O_2 on the surface of metallic materials was the following process: $* + H_2O_2 \rightarrow H_2O_2* \rightarrow 2HO* \rightarrow H_2O* + O*$, $O* + H_2TMB^{2+} \rightarrow OH* + HTMB^{2+} \rightarrow * + H_2O +$ oxTMB, and the desorption of HO*/O* and the oxidation of TMB to oxTMB were the key reaction steps (Ge et al., 2016; Li, Liu, Wu, & Gao, 2015; Xi et al., 2021). On the basis of it, different atom ratios of Au and Pt were built for four models to calculate the HO*/O* adsorption energy (Fig. S6). Fig. 3H showed that with the increase of Pt atom, the adsorption energy presented the volcano-type trend, which was based on the existence and increase of Au in the Pt cluster and the adsorption energies (E_{ads}) were utilized for OH and O as descriptors. $Au_{0.4}Pt_{0.6}$ surface had the weakest HO*/O* adsorption compared with other ratios. $E_{ads,\ OH}$ were − 2.031 eV (Au:Pt, 3:7), −2.032 eV (4:6), −2.196 eV (5:5) and − 2.269 eV (6:4), respectively. $E_{ads,\ O}$ were − 0.287 eV (3:7), −0.265 eV (4:6), −0.412 eV (5:5) and − 0.525 eV (6:4). Generally, the cluster vertex was occupied by Au atom as priority and the desorption of Au towards HO* and O* was relatively weak, so the adsorption site and calculation were on the basis of Pt atom in the cluster edge. With the increase of Au atom in cluster edges, the adsorption energy would lead to an obviously decrease, thus lowering the peroxidase-like activity. While we may not know the exaction of surface compositions of catalysts, the established models are enough to predict and explain the volcano-type activity trend with the increase of Au component in such as a unique system.

Besides, three catalyst modes of $Au_{0.3}Pt_{0.7}$, $Au_{0.4}Pt_{0.6}$, $Au_{0.5}Pt_{0.5}$ with different catalytical activities were constructed to explore the catalytic reaction mechanism of TMB on the Au_xPt_y surface. Based on the reaction process (Fig. 3F) and equations, the reaction routes and barriers of three catalyst models for the oxidation of TMB by H_2O_2 were identified and calculated. As shown in Fig. 3G, in the first adsorption step of H_2O_2, $Au_{0.3}Pt_{0.7}$ and $Au_{0.4}Pt_{0.6}$ both exhibited the barriers with energies of −0.05 eV, and $Au_{0.5}Pt_{0.5}$ was −0.14 eV. The adsorbed H_2O_2 could be easily reactivated and transferred to 2HO* without energy barriers on the all Au_xPt_y surface. However, the energies from 2HO* to O* on the surface of three catalyst models were 1.10 eV, 1.09 eV, 1.16 eV, respectively. In the following step, the surface O* captured two H atoms from H_2TMB^{2+} to form oxTMB and H_2O to complete the catalytic reaction. It was observed from the entire catalytic process that $Au_{0.4}Pt_{0.6}$ exhibited relatively better catalytic capacity.

3.5. Optimization of prepared conditions

Different concentrations of ILs assembled hydrogel were optimized to observe the loading of AuPt nanoparticles. Meanwhile, the absorbance using the hydrogel before and after recognizing ZEN was also investigated. In addition, the time-dependent of hydrogels when ZEN competes with cDNA was also studied. As shown in Fig. 4A, at the same condition, with ZEN, the absorbance was obviously higher than that before recognizing ZEN. It also demonstrated that ZEN would combine with aptamer desorbed from cDNA to release AuPt nanoparticles enclosed in the hydrogel. It also can be observed that the absorbance were differences with different ILs concentrations. The increased ILs content would bring the dense structure to be difficulty in loading more AuPt nanoparticles and making it difficult to release AuPt nanoparticles. And the poor hydrophilicity of lower ILs content would affect the modification of aptamer and cDNA, and the loading of AuPt nanoparticles. Therefore, 8% of ILs enhanced PAM/AA hydrogel was used to establish method.

Because the temperature would affect the structure and porosity of hydrogel, so the reaction temperature of ZEN with hydrogel was optimized. In this work, 4 °C, 25 °C and 50 °C were used as target competition temperature. It can be seen from Fig. 4B. that the absorbance value was relatively low at 4 °C and 25 °C compared with 50 °C, which presented the no obvious effect of reaction temperature. Therefore, the detection process was at room temperature considering the on-site testing of actual samples. The incubation time of this hydrogel sensor in the ZEN solution was also investigated. As shown in Fig. S7, with the increase of incubation time, the absorbance would increase, and the maximum absorbance value was detected at 30 min. Therefore, the optimized reacting time was 30 min.

3.6. Detection of ZEN

A colorimetric sensor was constructed by encapsulating Au_xPt_y nanozymes in hydrogel as a carrier. After adding ZEN, ZEN would preferentially combine with the aptamer to separate from cDNAs and further release AuPt nanoparticles. The separation ability of aptamer from cDNAs was positively correlated with ZEN concentration. The released AuPt nanoparticles would catalyze the TMB/H_2O_2 system and the solution changed from colorless to blue. Afterwards, a UV–Vis spectrophotometer was used to measure the absorbance value. It was found that the constructed sensor had a good response to different concentrations of ZEN. Fig. S8 showed a good linear relationship of the absorbance and ZEN concentration, and the linear range was 1–250 ng mL^{-1} with a limit of detection (LOD) of 0.6979 ng mL^{-1}. Table S1 compared the analytical performance of the established method and other literatures for ZEN detection. It could be seen that this method had a relatively low LOD, which was conducive to the detection of trace analytes.

To realize the rapid on-site detection, a smartphone was conducted for the further analysis. Images were captured by the smartphone, and the “Color Picker” application was utilized to recognize color and obtain R, G, and B values. They were processed and converted to the corresponding B/G value, which was consistent with the trend of the standard curve measured by the UV–Vis spectrophotometer. The smartphone-based method exhibited the linear range of 1–250 ng mL^{-1} with a LOD of 0.8941 ng mL^{-1} (Fig. 4E). Therefore, it could calculate the ZEN concentration to the B/G value in smartphone, which not only improved convenience but also further improved the limitation of being only suitable for laboratory use.

3.7. Specificity and anti-interference

To investigate the specific recognition ability of the established method towards ZEN, AFB1, PAT and OTA were selected as target analytes to be detected. As shown in Fig. 4C, the absorbance value of

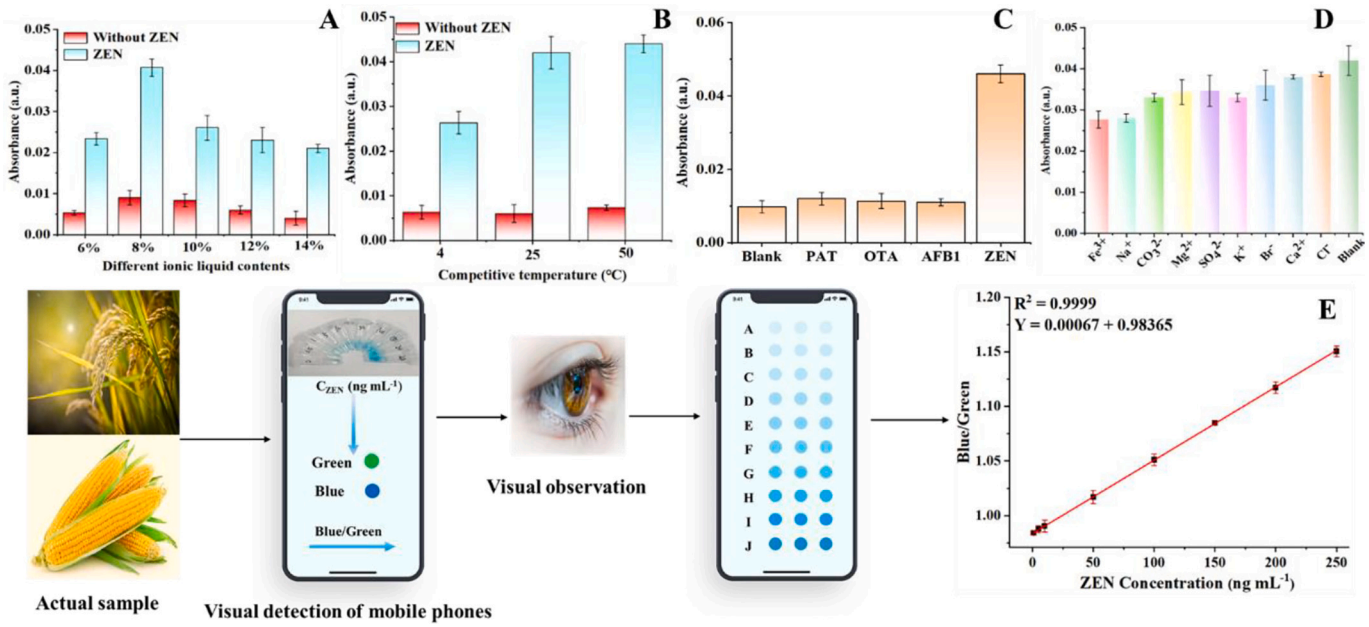

Fig. 4. (A) The influence of different IL contents on the absorbance. (B) The effect of different temperatures on the absorbance. (C) Selectivity of the colorimetric sensor towards ZEN (100 ng mL^{-1}) and other mycotoxins. (D) Research on anti-interference performance of colorimetric sensor. (E) Schematic diagram of smartphone detection.

ZEN was significantly higher than that of other three targets. The prepared PIL-AM/AA hydrogel colorimetric sensor showed no significant specificity towards other substances, which proved that the prepared colorimetric sensor has good specificity for the detection of ZEN. Besides, the anti-interference ability against other substances were also studied. Some inorganic ions including Fe^{3+}, Na^{+}, CO_3^{2-}, Mg^{2+}, SO_4^{2-}, K^{+}, Br^{-}, Ca^{2+}, Cl^{-} as interfering substances were added in the ZEN solution. As shown in Fig. 4D, when these substances were present, there was no significant impact on the absorbance, which proved that the prepared sensor has good anti-interference ability.

3.8. Real samples

Generally, ZEN exists in grains such as corn, wheat, sorghum, and rice that are susceptible to the fungal contamination. Corn and wheat were as samples to evaluate the application of this method. ZEN was detected in two samples, which was 2.35 ng mL^{-1} and 5.65 ng mL^{-1} in corn and wheat, respectively. It was not exceeding the national standard of People's Republic of China with the maximum residue limit of ZEN of 60 μg kg^{-1}. It indicated that the selected samples were contaminated to a certain extent. In order to evaluate the matrix interference, samples were spiked with different concentrations of standards to detect and calculate the recoveries. Table S2 presented that recoveries in wheat sample were in the range of 75.00%–100.00% and relative standard deviations (RSDs) were <10%. Recoveries of corn samples were ranging from 101.65% to 113.30% with RSDs ≤10%. Results showed that the established colorimetric biosensor with high anti-interference possessed good potential in food samples.

4. Conclusion

This study constructed an Au_xPt_y nanozymes-based colorimetric biosensor with PIL-PAM/AA hydrogel as the carrier. The hydrogel with 8% ILs had porous network structure and excellent mechanical properties. AuPt nanoparticles with excellent peroxidase activity were prepared and optimized. Through the kinetic analysis and theoretical calculation, it was found that $Au_{0.4}Pt_{0.6}$ nanoparticles exhibited an advantage over the decomposition of H_2O_2 to catalyze the TMB oxidation. Coupled with the smartphone application, this method presented a linear range of 1–250 ng mL^{-1} and a LOD of 0.6979 ng mL^{-1}. Due to the high specificity and good anti-interference ability, it was applied to detect ZEN in wheat and corn samples. Recoveries spiked with standards were 75.00%–100.00% of wheat and 101.65%–113.30% of corn, indicating the low matrix interference. Therefore, the hydrogel-based colorimetric method had a good potential in the on-site detection in food samples.

CRediT authorship contribution statement

Qianwen Liu: Visualization, Validation, Methodology, Data curation, Conceptualization. **Lingling Zhou:** Investigation. **Siyu Xin:** Data curation. **Wei Wu:** Investigation. **Qingli Yang:** Investigation, Data curation. **Xiudan Hou:** Writing – review & editing, Writing – original draft.

Declaration of competing interest

The authors declare that they have no known competing financial interests or personal relationships that could have appeared to influence the work reported in this paper.

Data availability

No data was used for the research described in the article.

Acknowledgment

This work was supported from Shandong Higher Education "Youth Innovation Team Plan" (2023), the Talents of High-Level Scientific Research Foundation, Qingdao Agricultural University (1119014), Postgraduate innovation gram of Qingdao Agricultural University (QNYCX22096), Rural Revitalization Science and Technology Innovation Plan Project of Shandong Province (2022TZXD0031), and Science & Technology Specific Projects in Agricultural High-tech Industrial Demonstration Area of the Yellow River Delta (2022SZX26).

Appendix A. Supplementary data

Supplementary data to this article can be found online at https://doi.org/10.1016/j.fochx.2024.101471.

References

Ahmadi, R., Azooz, E. A., Yamini, Y., & Ramezani, A. M. (2023). Liquid-liquid microextraction techniques based on in-situ formation/decomposition of deep eutectic solvents. *TrAC Trends in Analytical Chemistry, 161*, Article 117019. https://doi.org/10.1016/j.trac.2023.117019

Amor, I. B., Hemmami, H., Laouini, S. E., Ahmed, S., Mohammed, H. A., Abdullah, J. A. A., … Alharthi, F. (2023). Enhancing oxidant and dye scavenging through MgO-based chitosan nanoparticles for potential antioxidant coatings and efficient photocatalysts. *Biomass Conversion and Biorefinery*. https://doi.org/10.1007/s13399-023-04923-1

Bian, Y., Zhou, Z., Li, G., Liu, S., Li, S., Gao, Z., & Kang, W. (2023a). Bimetallic nanozymes laden DNA hydrogel for ultrasensitive optical detection of ractopamine. *Sensors and Actuators B: Chemical, 380*, Article 133402. https://doi.org/10.1016/j.snb.2023.133402

Fang, H., Wang, J., Li, L., Xu, L., Wu, Y., Wang, Y., Fei, X., Tian, J., & Li, Y. (2019). A novel high-strength poly(ionic liquid)/PVA hydrogel dressing for antibacterial applications. *Chemical Engineering Journal, 365*, 153–164. https://doi.org/10.1016/j.cej.2019.02.030

Gai, P., Pu, L., Wang, C., Zhu, D., & Li, F. (2023). CeO_2@NC nanozyme with robust dephosphorylation ability of phosphotriester: A simple colorimetric assay for rapid and selective detection of paraoxon. *Biosensors & Bioelectronics, 220*, Article 114841. https://doi.org/10.1016/j.bios.2022.114841

Gao, L., Zhuang, J., Nie, L., Zhang, J., Zhang, Y., Gu, N., … Yan, X. (2007). Intrinsic peroxidase-like activity of ferromagnetic nanoparticles. *Nature Nanotechnology, 2*(9), 577–583. https://doi.org/10.1038/nnano.2007.260

Gao, W., Chang, J., Li, X., Li, S., Zhou, Y., Hou, X., … Yuan, X. (2023). A quenched double-hydrophilic coating for the enhancement of water retention of hydrogels. *Advanced Functional Materials, 33*(31), Article 2303306. https://doi.org/10.1002/adfm.202303306

Ge, C., Fang, G., Shen, X., Chong, Y., Wamer, W. G., Gao, X., … Yin, J. (2016). Facet energy versus enzyme-like activities: The unexpected protection of palladium nanocrystals against oxidative damage. *ACS Nano, 10*(11), 10436–10445. https://doi.org/10.1021/acsnano.6b06297

Gilarska, A., Lewandowska-Łańcucka, J., Horak, W., & Nowakowska, M. (2018). Collagen/chitosan/hyaluronic acid–based injectable hydrogels for tissue engineering applications–design, physicochemical and biological characterization. *Colloids and Surfaces, B: Biointerfaces, 170*, 152–162. https://doi.org/10.1016/j.colsurfb.2018.06.004

Ji, W., Zhang, Z., Tian, Y., Yang, Z., Cao, Z., Zhang, L., … Wang, H. (2019). Shape coding microhydrogel for a real-time mycotoxin detection system based on smartphones. *ACS Applied Materials & Interfaces, 11*(8), 8584–8590. https://doi.org/10.1021/acsami.8b21851

Karimi-Maleh, H., Ranjbari, S., Tanhaei, B., Ayati, A., Orooji, Y., Alizadeh, M., … Sen, F. (2021). Novel 1-butyl-3-methylimidazolium bromide impregnated chitosan hydrogel beads nanostructure as an efficient nanobio-adsorbent for cationic dye removal: Kinetic study. *Environmental Research, 195*, Article 110809. https://doi.org/10.1016/j.envres.2021.110809

Khoris, I. M., Takemura, K., Lee, J., Hara, T., Abe, F., Suzuki, T., & Park, E. Y. (2019). Enhanced colorimetric detection of norovirus using in-situ growth of ag shell on au NPs. *Biosensors & Bioelectronics, 126*, 425–432. https://doi.org/10.1016/j.bios.2018.10.067

Li, J., Liu, W., Wu, X., & Gao, X. (2015). Mechanism of pH-switchable peroxidase and catalase-like activities of gold, silver, platinum and palladium. *Biomaterials, 48*, 37–44. https://doi.org/10.1016/j.biomaterials.2015.01.012

Li, W., Wang, Z., Wang, X., Cui, L., Huang, W., Zhu, Z., & Liu, Z. (2023). Highly efficient detection of deoxynivalenol and zearalenone in the aqueous environment based on nanoenzyme-mediated lateral flow immunoassay combined with smartphone. *Journal of Environmental Chemical Engineering, 11*(5), Article 110494. https://doi.org/10.1016/j.jece.2023.110494

Lu, Y., Qu, X., Wang, S., Zhao, Y., Ren, Y., Zhao, W., … Dong, X. (2022). Ultradurable, freeze-resistant, and healable MXene-based ionic gels for multi-functional electronic skin. *Nano Research, 15*(5), 4421–4430. https://doi.org/10.1007/s12274-021-4032-5

Lv, X., Liu, C., Shao, Z., Song, S., & Sun, S. (2020). Tailored ionic liquids encapsulation method endowing hydrogels with excellent mechanical and catalytic activity. *ACS Sustainable Chemistry & Engineering, 8*(15), 5975–5984. https://doi.org/10.1021/acssuschemeng.0c00409

Lv, X., Lv, A., Tian, S., Xie, T., & Sun, S. (2023). A tough and highly active catalyst carrier tailored by nanoparticles-encapsulation poly(ionic liquid) hydrogel: Synthesis and catalytic applications. *European Polymer Journal, 182*, Article 111713. https://doi.org/10.1016/j.eurpolymj.2022.111713

Lv, X., Tian, S., Liu, C., Luo, L., Shao, Z., & Sun, S. (2021). Tough, antibacterial and self-healing ionic liquid/multiwalled carbon nanotube hydrogels as elements to produce flexible strain sensors for monitoring human motion. *European Polymer Journal, 160*, Article 110779. https://doi.org/10.1016/j.eurpolymj.2021.110779

Ma, P., Guo, H., Ye, H., Zhang, Y., & Wang, Z. (2023). Aptamer-locker probe coupling with truncated aptamer for high-efficiency fluorescence polarization detection of zearalenone. *Sensors and Actuators B: Chemical, 380*, Article 133356. https://doi.org/10.1016/j.snb.2023.133356

Qiao, W., He, B., Yang, J., Ren, W., Zhao, R., Zhang, Y., Bai, C., Suo, Z., Xu, Y., Wei, M., & Jin, H. (2024). Pt@AuNF nanozyme and horseradish peroxidase-based lateral flow immunoassay dual enzymes signal amplification strategy for sensitive detection of zearalenone. *International Journal of Biological Macromolecules, 254*, Article 127746. https://doi.org/10.1016/j.ijbiomac.2023.127746

Qu, X., Liu, J., Wang, S., Shao, J., Wang, Q., Wang, W., … Zhao, Y. (2023). Photothermal regulated multi-perceptive poly(ionic liquids) hydrogel sensor for bioelectronics. *Chemical Engineering Journal, 453*, Article 139785. https://doi.org/10.1016/j.cej.2022.139785

Ramezani, A. M., Amiri Panah, F., Heydari Dokoohaki, M., Adnan Azooz, E., Ahmadi, R., & Nazari, S. (2024). Zn/Ce-layered double hydroxide for adsorptive removal of doxycycline from water. *Materials Chemistry and Physics, 318*, Article 129223. https://doi.org/10.1016/j.matchemphys.2024.129223

Semysim, F. A., Ridha, R. K., Azooz, E. A., & Snigur, D. (2024). Switchable hydrophilicity solvent-assisted solidified floating organic drop microextraction for separation and determination of arsenic in water and fish samples. *Talanta, 272*, Article 125782. https://doi.org/10.1016/j.talanta.2024.125782

Shao, J., Liu, M., Wang, Z., Li, K., Bao, B., Zhao, S., & Zhou, S. (2019). Controllable synthesis of surface Pt-rich bimetallic AuPt nanocatalysts for selective hydrogenation reactions. *ACS Omega, 4*(13), 15621–15627. https://doi.org/10.1021/acsomega.9b02117

Song, S., Li, N., Bai, L., Gai, P., & Li, F. (2022). Photo-assisted robust anti-interference self-powered biosensing of MicroRNA based on Pt–S bonds and the inorganic–organic hybridization strategy. *Analytical Chemistry, 94*(3), 1654–1660. https://doi.org/10.1021/acs.analchem.1c04135

Tan, X., Wang, X., Hao, A., Liu, Y., Wang, X., Chu, T., … Ming, D. (2020). Aptamer-based ratiometric fluorescent nanoprobe for specific and visual detection of zearalenone. *Microchemical Journal, 157*, Article 104943. https://doi.org/10.1016/j.microc.2020.104943

Tan, X., Xie, W., Jia, Q., Zhao, F., Wu, W., Yang, Q., & Hou, X. (2022). An aptamer and flower-shaped AuPtRh nanoenzyme-based colorimetric biosensor for the detection of profenofos. *Analyst, 147*(18), 4105–4115. https://doi.org/10.1039/d2an00668e

Wang, H., Lin, G., Li, X., Lu, W., & Peng, Z. (2019). Self-standing hollow porous AuPt nanospheres and their enhanced electrocatalytic performance. *Journal of Colloid and Interface Science, 554*, 396–403. https://doi.org/10.1016/j.jcis.2019.07.023

Wang, P., Cai, F., Li, Y., Yang, X., Feng, R., Lu, H., Bai, X., & Han, J. (2024). Emerging trends in the application of hydrogel-based biomaterials for enhanced wound healing: A literature review. *International Journal of Biological Macromolecules, 261*, Article 129300. https://doi.org/10.1016/j.ijbiomac.2024.129300

Wang, Y., Wang, S., Hu, W., Kong, S., Su, F., Liu, F., & Li, S. (2023). In situ hydrogels prepared by photo-initiated crosslinking of acrylated polymers for local delivery of antitumor drugs. *Journal of Pharmaceutical Sciences, 112*(7), 1863–1871. https://doi.org/10.1016/j.xphs.2023.02.004

Wei, D., Zhang, X., Chen, B., & Zeng, K. (2020). Using bimetallic au@Pt nanozymes as a visual tag and as an enzyme mimic in enhanced sensitive lateral-flow immunoassays: Application for the detection of streptomycin. *Analytica Chimica Acta, 1126*, 106–113. https://doi.org/10.1016/j.aca.2020.06.009

Wu, F., Wang, H., Lv, J., Shi, X., Wu, L., & Niu, X. (2023). Colorimetric sensor array based on Au2Pt nanozymes for antioxidant nutrition quality evaluation in food. *Biosensors and Bioelectronics, 236*, Article 115417. https://doi.org/10.1016/j.bios.2023.115417

Xi, Z., Wei, K., Wang, Q., Kim, M. J., Sun, S., Fung, V., & Xia, X. (2021). Nickel–platinum nanoparticles as peroxidase mimics with a record high catalytic efficiency. *Journal of the American Chemical Society, 143*(7), 2660–2664. https://doi.org/10.1021/jacs.0c12605

Yang, Y., Wu, D., Liu, J., Su, Z., Li, L., Wu, Y., & Li, G. (2022). High-efficiency enzyme-free catalyzed hairpin assembly-mediated homogeneous SERS and naked-eyes dual-mode assay for ultrasensitive and portable detection of mycotoxin. *Biosensors & Bioelectronics, 214*, Article 114526. https://doi.org/10.1016/j.bios.2022.114526

Zhang, L., Chen, J., Lu, L., Yu, R., & Zhang, D. (2023). A smartphone-assisted colorimetric aptasensor based on aptamer and gold nanoparticles for visual, fast and sensitive detection of ZEN in maize. *Food Chemistry: X, 19*, Article 100792. https://doi.org/10.1016/j.fochx.2023.100792

Zhou, Y., Fei, X., Tian, J., Xu, L., & Li, Y. (2022). A ionic liquid enhanced conductive hydrogel for strain sensing applications. *Journal of Colloid and Interface Science, 606*, 192–203. https://doi.org/10.1016/j.jcis.2021.07.158